

# The external field effect in cold dark matter models

Aseem Paranjape<sup>1\*</sup> & Ravi K. Sheth<sup>2,3†</sup>,

<sup>1</sup> *Inter-University Centre for Astronomy & Astrophysics, Ganeshkhind, Post Bag 4, Pune 411007, India*

<sup>2</sup> *Center for Particle Cosmology, University of Pennsylvania, 209 S. 33rd St., Philadelphia, PA 19104, USA*

<sup>3</sup> *The Abdus Salam International Center for Theoretical Physics, Strada Costiera, 11, Trieste 34151, Italy*

2 December 2021

## ABSTRACT

In general relativity (GR), the internal dynamics of a self-gravitating system under free-fall in an external gravitational field should not depend on the external field strength. Recent work has claimed a statistical detection of an ‘external field effect’ (EFE) using galaxy rotation curve data. We show that large uncertainties in rotation curve analyses and inaccuracies in published simulation-based external field estimates compromise the significance of the claimed EFE detection. We further show analytically that a qualitatively similar statistical signal is, in fact, expected in a  $\Lambda$ -cold dark matter ( $\Lambda$ CDM) universe without any violation of the strong equivalence principle. Rather, such a signal arises simply because of the inherent correlations between galaxy clustering strength and intrinsic galaxy properties. We explicitly demonstrate the effect in a baryonified mock catalog of a  $\Lambda$ CDM universe. Although the detection of an EFE-like signal is not, by itself, evidence for physics beyond GR, our work shows that the *sign* of the EFE-like correlation between the external field strength and the shape of the radial acceleration relation can be used to probe new physics: e.g., in MOND, the predicted sign is opposite to that in our  $\Lambda$ CDM mocks.

**Key words:** galaxies: formation - cosmology: theory, dark matter - methods: analytical, numerical

## 1 INTRODUCTION

The rotation curves of spiral galaxies, and more recently the velocity dispersion profiles of elliptical galaxies, show that the acceleration  $a_{\text{tot}}$  one infers from the observed motions of their stars or cold gas differs from the acceleration  $a_{\text{bary}}$  which one estimates from their observed baryonic mass distribution, if one assumes the motions are driven by Newtonian gravity. Nevertheless, the two accelerations define a rather tight correlation (McGaugh et al. 2016; Janz et al. 2016; Lelli et al. 2017; Chae et al. 2019; Tian et al. 2020; Chae et al. 2020), which is known as the radial acceleration relation (hereafter RAR). In cold dark matter (CDM) dominated models, Newtonian gravity is an excellent approximation, so both the shape and tightness of the RAR must emerge from the mixing of the baryonic and dark matter components as a galaxy’s stars form and its mass is assembled. In Modified Newtonian Dynamics (MOND, Milgrom 1983; Bekenstein & Milgrom 1984), which assumes there is no dark matter component, the RAR is a consequence of the departure from the Newtonian force law at small accelerations  $|\mathbf{a}| \ll a_0$ , with  $a_0 \sim 10^{-10} \text{ m s}^{-2}$  being a fundamental acceleration scale postulated in the theory. So, while the exact shape of the RAR depends on precisely how the gravitational force is modified, its tightness is ‘natural’. Both approaches are able to describe the observed shape and tightness of the RAR (see Paranjape & Sheth 2021, hereafter

PS21, and references therein). The observed median RAR is well described by  $a_{\text{tot}}/a_{\text{bary}} = \mathcal{F}(a_{\text{bary}}/a_0)$  where

$$\mathcal{F}(x) = \left[ \frac{1}{2} + \sqrt{\frac{1}{4} + \frac{1}{x^\nu}} \right]^{1/\nu}, \quad (1)$$

with  $a_0 = 1.2 \times 10^{-10} \text{ m s}^{-2}$  and  $\nu \simeq 0.8\text{--}1$  (Chae et al. 2019, 2020).

In general relativity (GR), the central assumption of the strong equivalence principle (SEP) means that the internal dynamics of a self-gravitating system under free-fall in an external gravitational field does not depend on the strength of the external field. However, MOND violates the SEP (see Bekenstein & Milgrom 1984, who presented a Lagrangian formulation of the theory) and consequently predicts an external field effect (EFE, Milgrom 1983). Consider a self-gravitating object, such as a star in a galaxy or a galaxy in the cosmic web, which experiences an external gravitational field  $\mathbf{a}_{\text{ext}}$  (whose tidal influence is assumed to be negligible). At sufficiently large distances from the object and in its center-of-mass rest frame, the EFE manifests as an effective dependence of Newton’s constant  $G_{\text{N}}$  on  $\mathbf{a}_{\text{ext}}$ , with the gravitational force experienced by a test particle in this frame being approximately Newtonian (and not MOND-ian) but with  $G_{\text{N}} = G_{\text{N}}(|\mathbf{a}_{\text{ext}}|)$  (e.g., equation 32 of Bekenstein & Milgrom 1984). If  $|\mathbf{a}_{\text{ext}}| \ll a_0$ , the modified  $G_{\text{N}}$  scales like  $\sim a_0/|\mathbf{a}_{\text{ext}}|$ .

Generic solutions of the field equations of MOND (and hence the EFE) relevant for galactic rotation curves have also been discussed in the literature (see, e.g., Milgrom 1986 for early work and Famaey & McGaugh 2012 for a recent

\* E-mail: aseem@iucaa.in

† E-mail: shethrk@physics.upenn.edu

review). While the 3-dimensional case requires numerical integration, in 1 dimension one can derive analytical solutions (see, e.g., section 6.3 and equation 59 of [Famaey & McGaugh 2012](#)). These have been used in the literature as heuristic approximations to search for observational signatures of the EFE ([Lelli et al. 2015](#); [Haghi et al. 2016, 2019](#); [Chae et al. 2020](#)).

Recent work has claimed a statistical detection ([Chae et al. 2020](#), hereafter, C20; see also [Chae et al. 2021a](#) and [Chae et al. 2021b](#)) in a subsample of 148 disk galaxies taken from the SPARC sample ([Lelli et al. 2016](#)). This detection boils down to noticing

- (i) a systematic departure from the RAR at low accelerations if no EFE is assumed (i.e. from equation 1), and
- (ii) a correlation of this departure with the external environment.

The EFE predicts that the RAR of an individual galaxy will deviate from equation (1) by an amount determined by  $\mathbf{a}_{\text{ext}}$ ; in the heuristic approaches mentioned above, this departure is a dip below (1) that becomes larger as the strength  $|\mathbf{a}_{\text{ext}}|$  of the external field increases.

The main goal of the present study is to show that a *statistical* EFE-like signal is, in fact, generically expected in CDM models when using realistic galaxy rotation curves. For this purpose, in addition to analytical arguments, we will use a mock galaxy catalog which [PS21](#) showed is able to describe the other aspects of the RAR. We will focus on the low-acceleration regime  $a_{\text{bary}} \leq 10^{-10} \text{ m s}^{-2}$  where the difference between setting  $\nu = 0.8$  or  $\nu = 1$  in equation (1) is negligible. The paper is organised as follows. In section 2, we present a simple but generic analytical calculation which demonstrates the existence of a statistical EFE in CDM models. In section 3, we describe our mock catalog, and present our numerical results. Section 4 presents a comparison with the literature, highlighting differences in how measurement uncertainties are incorporated into the analysis, and how the external field strength is estimated. We conclude in section 5.

Throughout,  $R_{\text{vir}}$  refers to the spherical radius around the host halo center-of-mass which encloses a total matter density 200 times the critical density  $\rho_{\text{crit}}$  of the Universe, while  $m_{\text{vir}}$  denotes the total mass enclosed inside this radius.

## 2 ANALYTICAL EXPECTATIONS

To understand what an ‘external field effect’ might look like in CDM models, we calculate the acceleration on the galaxy in question (which resides in a host halo of radius  $R_{\text{vir}}$ ) due to the mass external to  $R_{\text{vir}}$ .

Consider an arbitrary external matter distribution with overdensity  $\Delta(\mathbf{r}) = 1 + \delta(\mathbf{r}) = \rho(\mathbf{r})/\bar{\rho}$  given by the multipole expansion

$$\Delta(\mathbf{r}) - 1 = \Theta(r - R_{\text{vir}}) \sum_{\ell=0}^{\infty} \sum_{m=-\ell}^{\ell} \Delta_{\ell m}(r) Y_{\ell}^m(\hat{r}), \quad (2)$$

where  $\Theta(x)$  is the Heaviside step function and  $Y_{\ell}^m(\hat{r})$  are spherical harmonics.<sup>1</sup> One can derive the following exact relation

<sup>1</sup> Our convention is formally equivalent to assuming a uniform matter density at  $r < R_{\text{vir}}$ . It is straightforward to replace this

for  $\mathbf{a}_{\text{ext}}$  by solving Poisson’s equation  $\nabla^2 \phi^{(\text{ext})} = 4\pi G \bar{\rho}(\Delta - 1)$  for the potential  $\phi^{(\text{ext})}$  in spherical polar coordinates (e.g., [Binney & Tremaine 1987](#)) and evaluating its gradient at the origin:

$$\begin{aligned} \mathbf{a}_{\text{ext}} &= -\nabla \phi^{(\text{ext})}(\mathbf{r} = 0) \\ &= \sqrt{\frac{3}{16\pi}} \Omega_{\text{m}} H^2 \left[ \hat{z} \mathcal{D}_{10} - \sqrt{2} (\hat{x} \text{Re}(\mathcal{D}_{11}) - \hat{y} \text{Im}(\mathcal{D}_{11})) \right], \end{aligned} \quad (3)$$

where we defined the integrals

$$\mathcal{D}_{1m} \equiv \int_{R_{\text{vir}}}^{\infty} dr \Delta_{1m}(r), \quad (4)$$

used the fact that  $\Delta_{10}$  is real,  $\Delta_{1,-1} = -\Delta_{11}^*$  and made the associations  $\hat{r} = \hat{z}$ ,  $\hat{\theta} = \hat{x}$  and  $\hat{\phi} = \hat{y}$  at the origin of coordinates. Thus, for an arbitrary inhomogeneous external matter distribution, it is only the  $\ell = 1$  terms that contribute to an external field at the origin. The remaining terms vanish either due to symmetry (as in the case of the monopole  $\ell = 0$ ) or because they scale like positive powers of  $r \rightarrow 0$ . This trivially recovers the well-known result that  $\mathbf{a}_{\text{ext}}$  at the origin in Newtonian gravity vanishes for a perfectly spherical external mass distribution. It also shows that an axisymmetric dipolar mass field with  $\delta(\mathbf{r}) = \Delta_{10}(r) Y_1^0(\hat{r}) \sim \Delta_{10}(r) \cos(\theta)$  will lead to an external field  $\mathbf{a}_{\text{ext}}$  aligned with the dipole axis  $\hat{z}$ .

Dynamically, of course, this still does not explain why internal quantities such as the rotation curve of the galaxy should depend on  $\mathbf{a}_{\text{ext}}$  (apart from a trivial dependence on the chosen boundary at  $r = R_{\text{vir}}$ ). To see what equation (3) implies *statistically*, we first relate the multipole coefficients of the external matter field to its Fourier transform. Using the orthogonality of the spherical harmonics and the multipole expansion of the exponential  $e^{i\mathbf{k}\cdot\mathbf{r}} = 4\pi \sum_{\ell=0}^{\infty} i^{\ell} j_{\ell}(kr) \sum_{m=-\ell}^{\ell} Y_{\ell}^{m*}(\hat{k}) Y_{\ell}^m(\hat{r})$ , where  $j_{\ell}$  are spherical Bessel functions, leads to the relation  $\Delta_{\ell m}(r) = 4\pi i^{\ell} \int d^3k / (2\pi)^3 \delta_{\mathbf{k}} j_{\ell}(kr) Y_{\ell}^{m*}(\hat{k})$  in terms of the Fourier transform  $\delta_{\mathbf{k}} = \int d^3r e^{-i\mathbf{k}\cdot\mathbf{r}} \delta(\mathbf{r})$ . This in turn gives

$$\mathcal{D}_{1m} = 4\pi i \int \frac{d^3k}{(2\pi)^3} Y_1^{m*}(\hat{k}) k^{-1} j_0(kR_{\text{vir}}) \delta_{\mathbf{k}}, \quad (5)$$

where we used  $\int_A^{\infty} dx j_1(x) = j_0(A)$ , so that

$$\langle \mathcal{D}_{1m} \mathcal{D}_{1m}^* \rangle = \frac{2}{\pi} \int_0^{\infty} dk j_0(kR_{\text{vir}})^2 P_{\text{mm|g}}(k), \quad (6)$$

independent of  $m$ , where we used  $\int d\Omega_{\hat{k}} |Y_{\ell}^m(\hat{k})|^2 = 1$  and where  $P_{\text{mm|g}}(k)$  is the power spectrum of the mass external to the galaxy (i.e., conditioned on there being a galaxy at the center). This finally leads to the expectation value,

$$\langle \mathbf{a}_{\text{ext}} \cdot \mathbf{a}_{\text{ext}} \rangle = \left( \frac{3\Omega_{\text{m}} H^2}{2} \right)^2 \int_0^{\infty} \frac{dk}{2\pi^2} j_0(kR_{\text{vir}})^2 P_{\text{mm|g}}(k). \quad (7)$$

Although formally a 2-point quantity,  $P_{\text{mm|g}}(k)$  is essentially a galaxy-mass-mass bispectrum, and we finally see why rotation curves might be expected to correlate with  $\mathbf{a}_{\text{ext}}$ . This is simply because rotation curves depend on galaxy properties such as host halo mass, *as does* the large-scale clustering implied by  $P_{\text{mm|g}}(k)$ , e.g., through the galaxy’s linear bias  $b_1$  which we

with any other internal distribution if needed, ensuring appropriate boundary conditions at  $r = R_{\text{vir}}$ , without affecting the conclusions regarding  $\mathbf{a}_{\text{ext}}$ .

discuss below (see Desjacques et al. 2018, for a review). CDM models therefore implicitly contain a *statistical* external field effect.

To see how this manifests in the RAR, we turn to a numerical study using a mock catalog of galaxy rotation curves in the next section.

### 3 NUMERICAL RESULTS

#### 3.1 Mock catalog

Our mock catalog is the same as used by PS21 and is based on the algorithm described by Paranjape et al. (2021, hereafter, PCS21). We briefly describe the key features of the mock relevant to our analysis here, and refer the reader to PS21 and PCS21 for further details of the mock algorithm and underlying  $N$ -body simulation.

The catalog represents a luminosity-complete sample of galaxies with  $r$ -band absolute magnitude  $M_r \leq -19$  in a  $(300h^{-1}\text{Mpc})^3$  comoving volume at  $z = 0$ . The mock contains both central and satellite galaxies, populated in dark matter haloes identified in an  $N$ -body simulation having  $1024^3$  particles with a flat  $\Lambda$ CDM WMAP7 cosmology (Komatsu et al. 2011;  $\Omega_m = 0.276$ ,  $h = 0.7$ ). To achieve the luminosity completeness threshold of  $M_r \leq -19$ , haloes containing  $\geq 40$  particles are considered. Since the halo concentration cannot be reliably measured for haloes with fewer than about  $\sim 400$  particles, we use the method presented by Ramakrishnan et al. (2021) to assign concentrations  $c_{\text{vir}}$  (assuming Navarro et al. 1996, NFW profiles) conditioned on the mass and local tidal environment of individual haloes.<sup>2</sup> The galaxies were populated using a halo occupation distribution (HOD) model and HI-optical scaling relations calibrated by Paul et al. (2018) and Paul et al. (2019) using luminosity- and colour-dependent clustering measurements from the Sloan Digital Sky Survey (SDSS, York et al. 2000; Zehavi et al. 2011) and HI-dependent clustering measurements from the Arecibo Legacy Fast ALFA survey (ALFALFA, Giovanelli et al. 2005; Guo et al. 2017). Each galaxy in the mock is assigned absolute magnitudes in SDSS  $u$ ,  $g$  and  $r$  bands (with a threshold  $M_r \leq -19$  imposed by the SDSS clustering measurements) and a stellar mass  $m_*$  using a colour-dependent mass-to-light ratio. The HI-optical scaling relation additionally leads to a fraction  $\sim 60\%$  of galaxies to be assigned an HI mass  $m_{\text{HI}}$ . PCS21 presented extensive tests of this algorithm. We focus in this work on the population of mock central galaxies containing massive HI disks, with  $m_{\text{HI}} \geq 10^{9.7}h^{-2}M_\odot$ ; the resulting  $\sim 50,000$  such objects in our catalog form a volume-complete sample of HI-selected galaxies.

The host haloes of these centrals are ‘baryonified’ by the PCS21 algorithm using a modified version of the prescription of Schneider & Teyssier (2015). In addition to optical luminosity, colour, stellar mass and (where available) HI mass, each central galaxy system is further assigned spatial distributions of stars, cold gas, hot ionised gas, and gas ‘expelled’

due to feedback processes. The shapes of these distributions are observationally constrained; of relevance below are the distributions of stars and cold gas, which are respectively modelled as a Gaussian sphere with half-light radius  $R_{\text{HI}} \propto R_{\text{vir}}$  and an axisymmetric thin exponential disk with scale radius  $h_{\text{HI}} \propto m_{\text{HI}}^{0.5}$  (see PCS21 and PS21 for details and original references).

Finally, as discussed in detail by PS21, an important aspect of this ‘baryonification’ scheme as regards RAR studies is that the dark matter component of each baryonified halo is allowed to respond to the presence of its baryonic distribution by modelling a quasi-adiabatic relaxation process (Teyssier et al. 2011; Schneider & Teyssier 2015, see section 3 of PS21). This is done in a parametrised fashion using a ‘relaxation parameter’  $q_{\text{rdm}}$  to control the amount of quasi-adiabatic relaxation, such that  $q_{\text{rdm}} = 1$  ( $q_{\text{rdm}} = 0$ ) corresponds to perfect angular momentum conservation (no baryonic backreaction). The value  $q_{\text{rdm}} = 0.68$  provides a good description of the effect seen in cluster-sized haloes in hydrodynamical CDM zoom simulations (Teyssier et al. 2011; Schneider & Teyssier 2015), but is subject to some theoretical uncertainty as discussed by PS21, settling which requires a detailed study of hydrodynamical simulations of galaxy formation over a large mass range. In the following, we set  $q_{\text{rdm}} = 0.33$  when generating baryonified rotation curves; PS21 showed that this improves the agreement at high accelerations  $a_{\text{bary}} \geq 10^{-10} \text{ m s}^{-2}$  between the median RAR of our mock and equation (1) with  $\nu = 1$  (which Chae et al. 2020 argue provides a good description of the SPARC sample at similar  $a_{\text{bary}}$ ). At the low accelerations of our interest, however, our results are insensitive to  $q_{\text{rdm}}$  and are unchanged if we use the default value  $q_{\text{rdm}} = 0.68$  used by PS21.

#### 3.2 RAR and the environment in a CDM mock catalog

The observable that C20 attribute to an EFE is a downward deviation of the RAR of individual galaxies or the ensemble from equation (1). PS21 showed that, in CDM models, the objects which dominate the downturn in the RAR tend to have smaller masses. This is highlighted in Fig. 1 which shows the individual RARs of 150 galaxies randomly chosen from our full sample. Each curve in the *upper panel* is coloured by the total mass  $m_{\text{vir}}$  of the host halo, while the *lower panel* shows the same curves coloured by the stellar mass  $m_*$  of each galaxy. We clearly see the low- $m_{\text{vir}}$  objects in the *upper panel* falling below equation (1) (shown as the solid purple curve in each panel), while this correlation visibly weakens when using  $m_*$  in place of  $m_{\text{vir}}$  in the *lower panel*. This weakening is not surprising, considering the substantial scatter of the stellar mass-halo mass relation (see, e.g., fig. 12 of PCS21). The rotation curves used for evaluating  $a_{\text{tot}}$  and  $a_{\text{bary}}$  are sampled on 20 logarithmically spaced points in the range  $(10^{-3}, 1) \times R_{\text{vir}}$  for each galaxy. We have displayed each curve in the range  $r \leq 4.7h_{\text{HI}}$ , where  $h_{\text{HI}}$  is the scale length of the thin exponential HI disk assigned to each galaxy, with surface mass density of HI gas  $\Sigma_{\text{HI}}(r) \propto e^{-r/h_{\text{HI}}}$  in the disk plane. Since our model assumes  $h_{\text{HI}} \propto m_{\text{HI}}^{0.5}$ , this cut on  $r/h_{\text{HI}}$  corresponds to a column density threshold of  $N_{\text{HI}} \geq 10^{19.5} \text{ cm}^{-2}$ , which follows from writing  $N_{\text{HI}}(r) \simeq \Sigma_{\text{HI}}(r)/m_{\text{p}}$  ( $m_{\text{p}}$  being the proton mass) and represents a typical  $5\sigma$  limiting threshold for spatially resolved 21 cm spectroscopy (e.g., Begum & Chengalur 2004;

<sup>2</sup> The calibration of Ramakrishnan et al. (2021) assumes concentrations  $c_{200b} \equiv R_{200b}/r_s$ , where  $R_{200b}$  is the halo-centric radius which encloses a density 200 times the background value and  $r_s$  is the halo’s NFW scale radius. We convert these to  $c_{\text{vir}} \equiv R_{\text{vir}}/r_s$  using the analytical prescription of Hu & Kravtsov (2003).

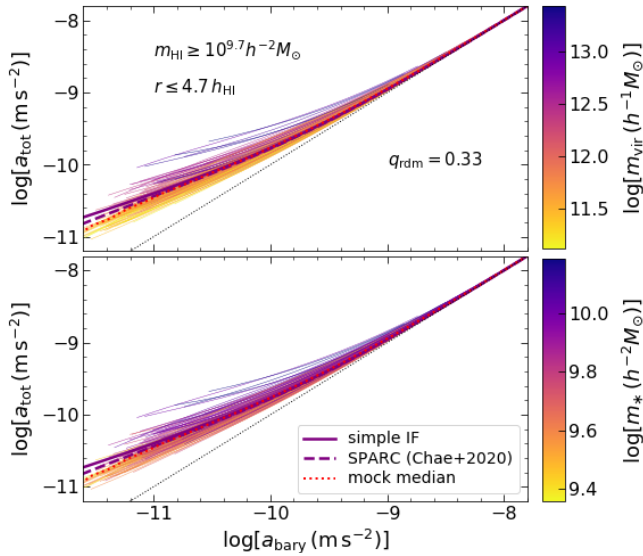


**Figure 1. RAR and halo/stellar mass.** Radial acceleration relation (RAR) for 150 massive spiral galaxies selected randomly from a volume-complete mock catalog with  $M_r \leq -19$  and  $m_{\text{HI}} \geq 10^{9.7} h^{-2} M_{\odot}$ . Thin curves show the RARs of individual galaxies coloured by host halo mass  $m_{\text{vir}}$  (*top panel*) and stellar mass  $m_*$  (*bottom panel*). Each rotation curve is truncated at  $r \leq 4.7 h_{\text{HI}}$  to mimic an observational column density threshold of  $N_{\text{HI}} \geq 10^{19.5} \text{ cm}^{-2}$ . In each panel, the solid purple curve shows equation (1) setting  $\nu = 1$ , the dashed purple curve shows equation (6) of C20 setting their parameter  $e = 0.032$ , the dotted red curve shows the median RAR of the full volume-complete sample (containing  $\sim 50,000$  galaxies) and the thin dotted black line shows the 1:1 relation. See text for a discussion.

Battaglia et al. 2006; Chemin et al. 2006; Boomsma et al. 2008).

The dashed purple curve in each panel shows the RAR derived from equation (6) of C20, setting their parameter  $e = 0.032$ , which they showed describes the median RAR of the SPARC sample at  $a_{\text{bary}} \lesssim 10^{-11} \text{ m s}^{-2}$  somewhat better than does equation (1). For comparison, the dotted red curve in each panel shows the median RAR of our entire volume-complete mock sample. Like the dashed purple curve, the median RAR of our mock also dips below equation (1) at low  $a_{\text{bary}}$ . The RARs of the individual galaxies show that this is driven by the low-mass host halos. The individual RARs also depend on halo concentration: we discuss this in more detail in the next subsections. For reference, the median along with 16<sup>th</sup> and 84<sup>th</sup> percentiles of  $\log[m_{\text{vir}}(h^{-1} M_{\odot})]$  for this sample are  $11.88^{+0.66}_{-0.44}$ . We have checked that our results are robust against varying the cut on  $r/h_{\text{HI}}$  between  $\sim 3.5$ -6, corresponding to column density thresholds of  $\sim 10^{19}$ - $10^{20} \text{ cm}^{-2}$ .

### 3.2.1 RAR and large-scale halo bias

Since halo mass and concentration in the CDM paradigm correlate with large-scale environment, the discussion above shows that we would also expect the galaxies dipping below equation (1) in Fig. 1 to have smaller values of linear bias  $b_1$ . We test this expectation as follows. As a proxy for the EFE observable, for each object in the mock catalog, we first

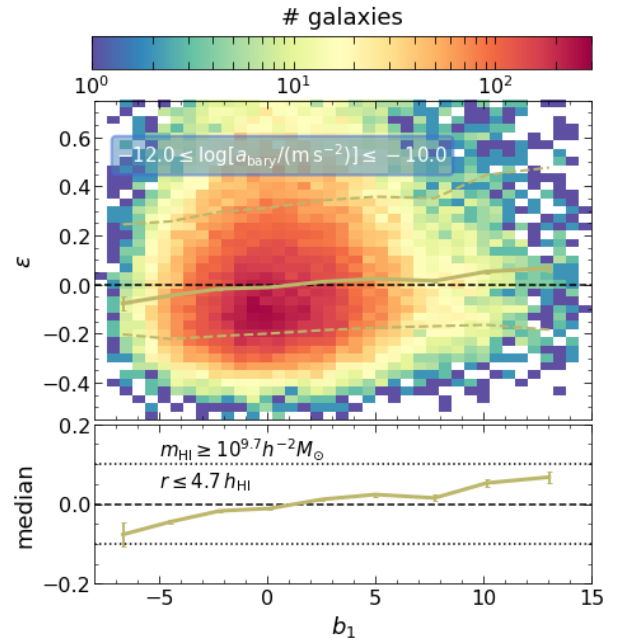


**Figure 2. Statistical EFE in CDM.** (*Top panel*): Joint distribution of  $\epsilon$  defined in equation (8), which measures a departure from the median RAR, and galaxy linear bias  $b_1$  in the same mock catalog containing  $\sim 50,000$  galaxies used for Fig. 1. Dashed black horizontal line shows the median value of  $\epsilon$  (essentially zero) in the mock catalog. Solid yellow line shows the median  $\epsilon$  in bins of  $b_1$ , with error bars calculated using 150 bootstrap samples. Dashed yellow lines show the 16<sup>th</sup> and 84<sup>th</sup> percentiles of  $\epsilon$  in the same  $b_1$  bins. (*Bottom panel*): Zoom-in view of the solid yellow line. Dotted horizontal lines show  $\pm 10\%$  variations around zero (shown by the dashed horizontal line). A weak but significant positive trend is apparent in the median  $\epsilon$  as a function of  $b_1$ .

estimate

$$\epsilon \equiv \left\langle \left[ \frac{a_{\text{tot}}}{a_{\text{tot,med}}(a_{\text{bary}})} - 1 \right] \right\rangle, \quad (8)$$

where  $a_{\text{tot,med}}(a_{\text{bary}})$  is the median  $a_{\text{tot}}$  measured in narrow bins of  $a_{\text{bary}}$  using all galaxies in our sample, and interpolated to the value of  $a_{\text{bary}}$  for each galaxy. The angular brackets indicate, for each galaxy, the median over data points for which  $10^{-12} \leq a_{\text{bary}}/(m s^{-2}) \leq 10^{-10}$  and  $r \leq 4.7 h_{\text{HI}}$  (see above). Using the mean or minimum instead of the median in defining the angular brackets leads to very similar results, as does varying the cut on  $r/h_{\text{HI}}$  between  $\sim 3.5$ -6 (see above). Since  $\epsilon$  is averaged over a wide range of  $a_{\text{bary}}$ , it is a measure of the overall offset of a galaxy's RAR from the sample median, and does not distinguish between differences in shape or amplitude of the RAR. In contrast, the parameter  $e$  used by C20 and which we discuss later, is intended to quantify differences in RAR shape, although in practice the best-fit  $e$  for any galaxy may depend on whether the acceleration scale  $a_0$  is also treated as a free parameter.

In addition, for each object we estimate the linear bias  $b_1$ , following Paranjape et al. (2018), as a proxy for the large-scale environment. The *top panel* in Fig. 2 shows  $\epsilon$  vs  $b_1$  for our sample (all these objects have at least one value of  $a_{\text{bary}}$  between  $10^{-12} - 10^{-10} \text{ m s}^{-2}$  such that  $r \leq 4.7 h_{\text{HI}}$ ). The solid yellow line shows the median  $\epsilon$  for narrow bins in  $b_1$ , and

dashed yellow lines show the region which encloses 68% of the objects. There is a clear trend with  $b_1$ , which the *bottom panel* zooms in on. Evidently, the median  $\varepsilon$  in the most overdense environments is weakly but significantly higher than that in the most underdense ones, with a  $\sim 15\%$  overall change from  $b_1 \sim -7$  to  $b_1 \sim 12$ . Mean density environments have median  $\varepsilon \simeq 0$ . We find a Spearman correlation coefficient of  $+0.08$  between  $\varepsilon$  and  $b_1$ , with negligible  $p$ -value, consistent with the median trend. This qualitative trend is consistent with the expectations from the RAR analysis mentioned above: galaxies which dip below equation (1) have preferentially smaller values of  $b_1$ .

We have also explicitly checked that the trend between  $\varepsilon$  and  $b_1$  disappears when evaluated at fixed host mass  $m_{\text{vir}}$  and concentration  $c_{\text{vir}}$ . We do this by rank-ordering  $b_1$  in joint percentiles of  $m_{\text{vir}}$  and  $c_{\text{vir}}$  and correlating the resulting ranks of  $b_1$  with  $\varepsilon$ . The resulting median  $\varepsilon$  is consistent with zero at fixed  $b_1$  rank, with errors similar to or smaller than those displayed in Fig. 2, and the Spearman correlation coefficient between  $\varepsilon$  and the  $b_1$  rank is  $+0.006$  with a  $p$ -value of 0.17, indicating no significant correlation. This emphasizes that  $\varepsilon$  and  $b_1$  are only correlated because each of them separately correlates with  $m_{\text{vir}}$  and  $c_{\text{vir}}$ . Interestingly, we also find that fixing  $m_{\text{vir}}$  alone decreases, but does not completely erase, the  $\varepsilon \leftrightarrow b_1$  correlation (Spearman correlation  $+0.05$  with negligible  $p$ -value), showing that halo assembly bias effects can leave (weak) imprints in RAR-environment correlations. We return to this point below.

### 3.2.2 RAR and the external acceleration field

In the context of equation (7), we expect that  $\varepsilon$  must also correlate with  $|\mathbf{a}_{\text{ext}}|$ . To test this, we measured  $\mathbf{a}_{\text{ext}}$  at each host halo location in our simulation box as the contribution of all mass in the radial shell  $R_{\text{vir}} \leq r \leq r_{\text{max}}$ . For ease of comparison with Desmond et al. (2018, hereafter, D18) who performed a similar study with a different technique, we set  $r_{\text{max}} = 10$  Mpc for our default analysis and comment on the scale dependence of our results later. In practice, we calculated  $\mathbf{a}_{\text{ext}}$  by summing over the vector accelerations induced by all dark matter particles in the radial shell centered on each halo, at the halo center:

$$\mathbf{a}_{\text{ext}} = \sum_{p \in \text{shell}} \frac{Gm_{\text{part}}\mathbf{x}_p}{x_p^3} = \frac{3\Omega_m H^2 L}{8\pi N_{\text{part}}} \sum_{p \in \text{shell}} \frac{\mathbf{r}_p}{r_p^3}, \quad (9)$$

where  $\mathbf{r}_p = \mathbf{x}_p/L$  is the halo-centric position vector of the  $p^{\text{th}}$  particle, normalised by the box size  $L$ , and  $N_{\text{part}}$  is the total number of particles in the simulation. To speed up the calculation, we first downsampled the particle distribution to  $256^3$  particles (from the native sampling of  $1024^3$  particles), replacing  $N_{\text{part}} \rightarrow 256^3$  in equation (9). We have checked using halo-based samples that our results are converged with respect to downsampling level.<sup>3</sup> Unlike the discrete halo counting employed by D18, which necessarily requires making assumptions regarding the mass contributed by unresolved halos in the

<sup>3</sup> We have also checked, using a  $(600h^{-1}\text{Mpc})^3$  simulation with  $1024^3$  particles, that our results for halos with  $m_{\text{vir}} \gtrsim 10^{12}h^{-1}M_{\odot}$  (including the correlations of  $\mathbf{a}_{\text{ext}}$  with halo mass and concentration discussed later) are converged with respect to box volume.

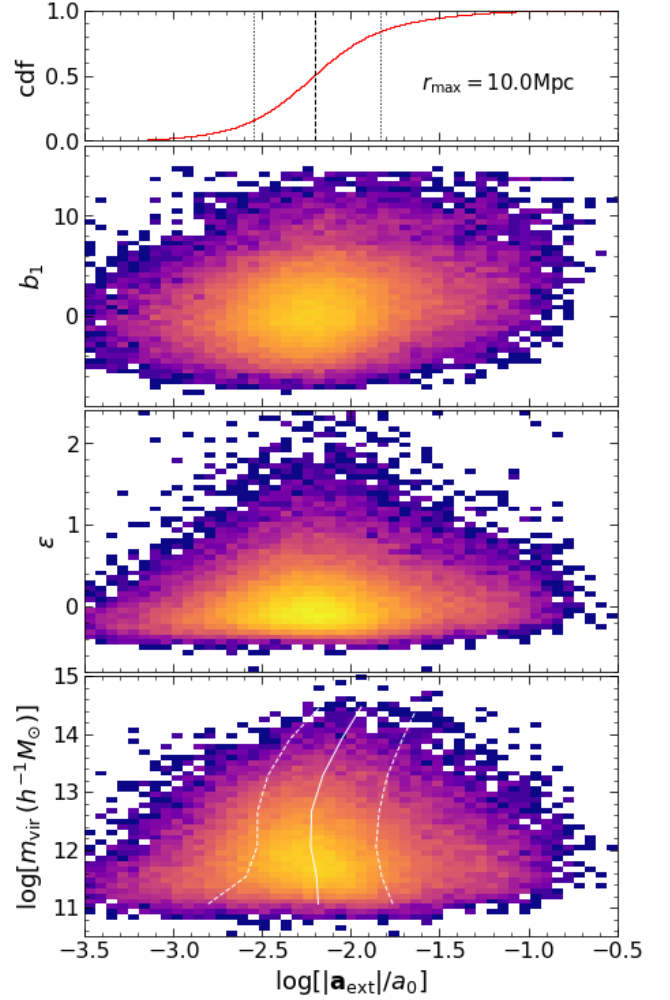


**Figure 3. Distribution of  $|\mathbf{a}_{\text{ext}}|$  for mock galaxies.** *Upper-most panel* shows the cumulative distribution of  $\log[|\mathbf{a}_{\text{ext}}|/a_0]$  estimated using  $r_{\text{max}} = 10$  Mpc as described in the text for the same mock galaxies used in Fig. 2. Vertical dashed and dotted lines indicate the median and central 68% region, respectively, of the distribution. Subsequent panels show, from *top to bottom*, the joint distribution of  $\log[|\mathbf{a}_{\text{ext}}|/a_0]$  with linear bias  $b_1$ , the RAR residual  $\varepsilon$  from equation (8) and host mass  $\log[m_{\text{vir}}]$ , with the colour indicating binned galaxy counts on a logarithmic scale (decreasing from yellow to purple). White solid line in the bottom panel shows the median  $\log[|\mathbf{a}_{\text{ext}}|/a_0]$  in bins of  $\log[m_{\text{vir}}]$ , with dashed white lines showing the corresponding central 68% region.

simulation box, our method correctly accounts for *all* mass in the desired radial shell; we return to this point in section 4.

Fig. 3 shows the cumulative distribution of  $\log[|\mathbf{a}_{\text{ext}}|/a_0]$  with  $a_0 = 1.2 \times 10^{-10} \text{ m s}^{-2}$  in the *upper-most panel*, followed by the joint distribution of  $\log[|\mathbf{a}_{\text{ext}}|/a_0]$  with  $b_1$ ,  $\varepsilon$  and  $\log[m_{\text{vir}}]$  (2-d histograms from top to bottom). The median  $|\mathbf{a}_{\text{ext}}|/a_0$  along with the central 68% range is  $(6.2_{-3.4}^{+8.4}) \times 10^{-3}$  (vertical lines in the *upper-most panel*). We see a relatively tight correlation between  $|\mathbf{a}_{\text{ext}}|$  and  $b_1$  (Spearman correlation coefficient  $\simeq +0.18$  with negligible  $p$ -value), consistent with expectations from equation (7). The corresponding correlation between  $|\mathbf{a}_{\text{ext}}|$  and  $\varepsilon$  (Spearman coefficient  $\simeq +0.08$  with negligible  $p$ -value) is similar to the one between  $b_1$  and  $\varepsilon$

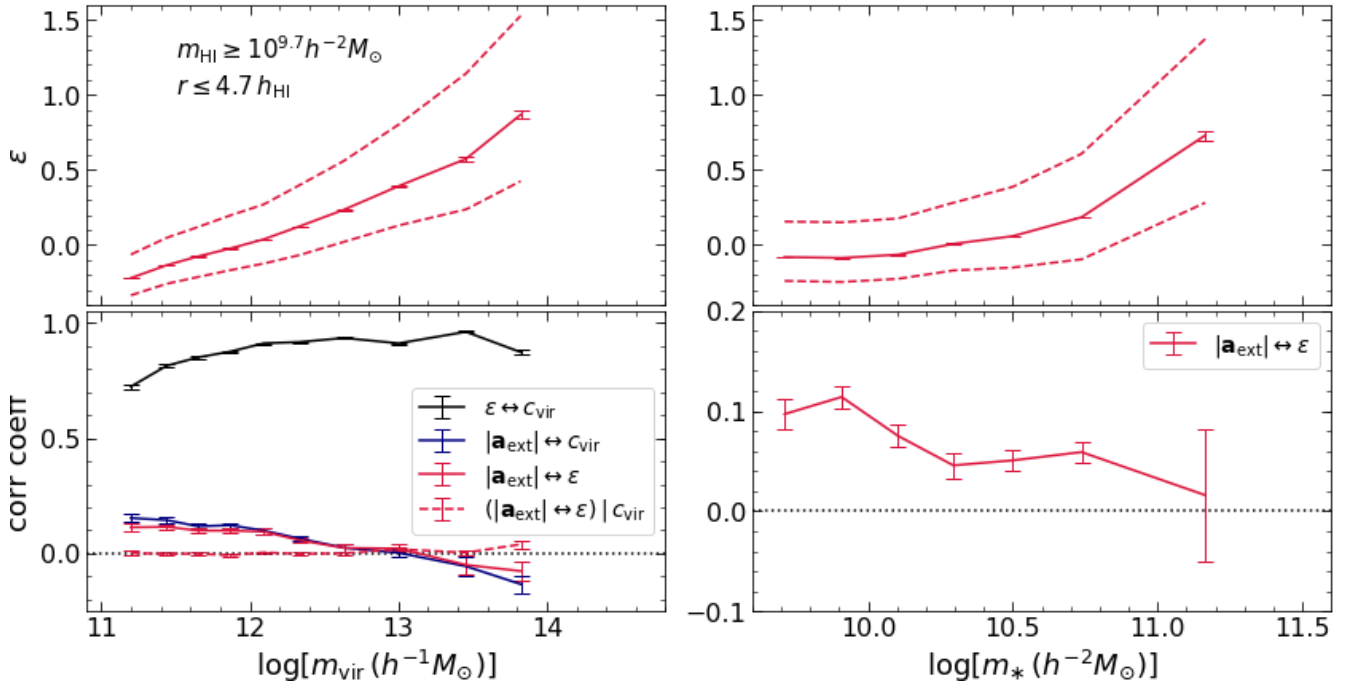


**Figure 4. Correlation between  $\varepsilon$  and  $|\mathbf{a}_{\text{ext}}|$  for mock galaxies.** (*Top left panel:*) Median (solid red) and central 68% region (dashed red) of the distribution of  $\varepsilon$  in bins of  $\log[m_{\text{vir}}]$  for the same mock galaxies used in Fig. 2. Both the median and the scatter in  $\varepsilon$  monotonically increase with  $m_{\text{vir}}$ . (*Bottom left panel:*) Solid lines show Spearman rank correlation coefficients between  $\varepsilon \leftrightarrow c_{\text{vir}}$  (black),  $|\mathbf{a}_{\text{ext}}| \leftrightarrow c_{\text{vir}}$  (blue) and  $|\mathbf{a}_{\text{ext}}| \leftrightarrow \varepsilon$  (red) in bins of  $m_{\text{vir}}$ . The latter two curves show a clear inversion of sign near  $m_{\text{vir}} \simeq 10^{13} h^{-1} M_{\odot}$ , which the text argues is a version of halo assembly bias. Dashed red line shows the conditional correlation coefficient  $\gamma_{(|\mathbf{a}_{\text{ext}}| \leftrightarrow \varepsilon) | c_{\text{vir}}}$  as defined in equation (10). This is nearly zero across the entire range of  $m_{\text{vir}}$ , an indication that the  $|\mathbf{a}_{\text{ext}}| \leftrightarrow \varepsilon$  correlation is driven by halo concentration  $c_{\text{vir}}$ . (*Top right panel:*) Median (solid red) and central 68% region (dashed red) of the distribution of  $\varepsilon$  in bins of  $\log$ -stellar mass  $\log[m_{*}]$  for the same mock galaxies. The trend with  $m_{*}$  is much shallower than that with  $m_{\text{vir}}$ , a consequence of the scatter in the  $m_{*}$ - $m_{\text{vir}}$  relation (see text). (*Bottom right panel:*)  $|\mathbf{a}_{\text{ext}}| \leftrightarrow \varepsilon$  correlation in bins of  $\log[m_{*}]$ . This remains positive for nearly all  $m_{*}$  explored in the mock. Error bars in all panels were computed as the scatter across 150 bootstrap realisations.

discussed above. The *lower-most panel* shows that  $|\mathbf{a}_{\text{ext}}|$  and host mass  $m_{\text{vir}}$  define a tight correlation at large  $m_{\text{vir}}$ , which is then inherited by  $\varepsilon$  through its  $m_{\text{vir}}$  dependence.

Fig. 4 explores the  $|\mathbf{a}_{\text{ext}}| \leftrightarrow \varepsilon$  correlation in more detail. Since the RAR residual  $\varepsilon$  correlates with the environment through its dependence on halo mass  $m_{\text{vir}}$  and concentration  $c_{\text{vir}}$ , it is natural to ask how its correlation with  $|\mathbf{a}_{\text{ext}}|$  is affected by these variables. For reference, the *top left panel* of the Figure shows the median and the region containing the central 68 percent of  $\varepsilon$  values in bins of  $m_{\text{vir}}$ , while the solid black curve in the *bottom left panel* shows the Spearman rank correlation coefficient  $\gamma_{\varepsilon c_{\text{vir}}}$  between  $\varepsilon$  and  $c_{\text{vir}}$ ; we see a clear monotonic increase in both the median and scatter of  $\varepsilon$  with  $m_{\text{vir}}$  and a strong positive  $\varepsilon \leftrightarrow c_{\text{vir}}$  correlation at fixed  $m_{\text{vir}}$ , as expected from the discussion in PS21 (see their fig. 6). The solid red line in the *bottom left panel* of Fig. 4 shows the Spearman coefficient  $\gamma_{|\mathbf{a}_{\text{ext}}| \varepsilon}$  between  $|\mathbf{a}_{\text{ext}}|$  and  $\varepsilon$  at fixed  $m_{\text{vir}}$ . We see a weak but significant correlation which is positive at low  $m_{\text{vir}}$  and changes sign at  $m_{\text{vir}} \gtrsim 10^{13} h^{-1} M_{\odot}$ .<sup>4</sup> This change of sign is reminiscent of the well-known  $b_1 \leftrightarrow c_{\text{vir}}$  assembly bias correlation at fixed  $m_{\text{vir}}$ , which similarly changes sign from positive to negative at  $m_{\text{vir}} \gtrsim 10^{13} h^{-1} M_{\odot}$

<sup>4</sup> We have checked that the values of  $\gamma_{|\mathbf{a}_{\text{ext}}| \varepsilon}$  vary by only a few percent at any  $m_{\text{vir}}$  when the cut on  $r/h_{\text{HI}}$  is varied between  $\sim 3.5$ -6 (see section 3.2).

(Wechsler et al. 2006; Faltenbacher & White 2010). Indeed, the solid blue line shows that the Spearman coefficient  $\gamma_{|\mathbf{a}_{\text{ext}}| c_{\text{vir}}}$  between  $|\mathbf{a}_{\text{ext}}|$  and  $c_{\text{vir}}$  also shows the same behaviour with  $m_{\text{vir}}$ . Since  $\varepsilon$  in our  $\Lambda$ CDM mock does not directly depend on the external environment, it is worth asking whether the *entire*  $|\mathbf{a}_{\text{ext}}| \leftrightarrow \varepsilon$  correlation can be explained by the separate correlations  $|\mathbf{a}_{\text{ext}}| \leftrightarrow c_{\text{vir}}$  and  $\varepsilon \leftrightarrow c_{\text{vir}}$ , at fixed  $m_{\text{vir}}$  (just like the  $b_1 \leftrightarrow \varepsilon$  correlation discussed earlier). To test this, we follow Ramakrishnan et al. (2019) and calculate the conditional correlation coefficient  $\gamma_{(|\mathbf{a}_{\text{ext}}| \leftrightarrow \varepsilon) | c_{\text{vir}}}$  defined as

$$\gamma_{(|\mathbf{a}_{\text{ext}}| \leftrightarrow \varepsilon) | c_{\text{vir}}} = \gamma_{|\mathbf{a}_{\text{ext}}| \varepsilon} - \gamma_{|\mathbf{a}_{\text{ext}}| c_{\text{vir}}} \gamma_{\varepsilon c_{\text{vir}}}, \quad (10)$$

which should vanish if  $|\mathbf{a}_{\text{ext}}|$  and  $\varepsilon$  are only correlated because of their individual correlations with  $c_{\text{vir}}$ . The dashed red line in the *bottom left panel* shows that this is indeed the case. This result is striking in its similarity to that for the  $b_1 \leftrightarrow \varepsilon$  correlation, and shows the potential of the  $|\mathbf{a}_{\text{ext}}| \leftrightarrow \varepsilon$  correlation in hunting for galaxy assembly bias.<sup>5</sup>

The sign of the  $|\mathbf{a}_{\text{ext}}| \leftrightarrow \varepsilon$  correlation is thus predicted to depend on  $m_{\text{vir}}$ . In practice, however, one is likely to assess

<sup>5</sup> This result also opens the door to investigating the *origin* of the  $|\mathbf{a}_{\text{ext}}| \leftrightarrow c_{\text{vir}}$  correlation. The results of Ramakrishnan et al. (2019), and the very definition of  $\mathbf{a}_{\text{ext}}$  as a derivative of the gravitational potential, suggest that this correlation might ultimately be explained by the tidal environment of the galaxy's host halo. We will pursue this question in future work.

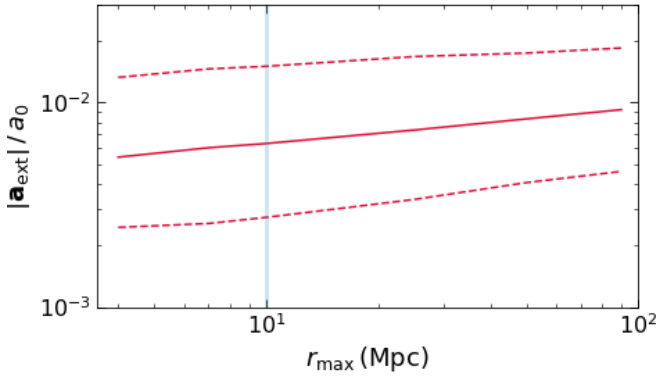


**Figure 5.** Scale dependence of  $|\mathbf{a}_{\text{ext}}|$  for the mock galaxies used in Fig. 3. Solid curve shows the median  $|\mathbf{a}_{\text{ext}}|/a_0$  as a function of  $r_{\text{max}}$ , while the dashed curves show the corresponding central 68% region of the distribution. Vertical line indicates  $r_{\text{max}} = 10$  Mpc, the default value used in the text.

this correlation as a function of quantities such as stellar mass  $m_*$ , which is easier to estimate than halo mass  $m_{\text{vir}}$ . The *bottom right* panel of Fig. 4 shows that, at fixed  $m_*$ ,  $\gamma_{|\mathbf{a}_{\text{ext}}| \leftrightarrow \varepsilon}$  is in fact positive over essentially the entire range of  $m_*$  probed by our mock catalog. Finally, the *top right panel* shows that the distribution of  $\varepsilon$  is a much weaker function of  $m_*$  than it is of  $m_{\text{vir}}$ . This is easy to understand in terms of the shape and scatter of the  $m_*$ - $m_{\text{vir}}$  relation (e.g., fig. 12 of PCS21). At any fixed  $m_* \lesssim 10^{10.5} h^{-2} M_{\odot}$ , the  $\varepsilon$  distribution in our mock catalog is averaged over a similar range of  $m_{\text{vir}} \sim 10^{11.5} - 10^{12.5} h^{-1} M_{\odot}$ , while at  $m_* \gtrsim 10^{10.5} h^{-2} M_{\odot}$  it is progressively averaged over larger  $m_{\text{vir}}$ , leading to the steepening seen in the plot.

Overall, then, our  $\Lambda$ CDM mock catalog predicts that the distribution of  $\varepsilon$  is a strong function of  $m_{\text{vir}}$  but a much weaker function of stellar mass  $m_*$  and, more interestingly for EFE analyses, that there is a *positive* correlation between  $\varepsilon$  and  $|\mathbf{a}_{\text{ext}}|/a_0$  for all systems but those with the highest  $m_{\text{vir}}$ , such that galaxies dipping below equation (1) tend to have *smaller*  $|\mathbf{a}_{\text{ext}}|$ . This trend between  $|\mathbf{a}_{\text{ext}}|$  and  $\varepsilon$  is also different from the MOND prediction where, in the language of C20, the variable  $e \sim -\varepsilon$  should correlate positively with  $e_{\text{env}} = |\mathbf{a}_{\text{ext}}|/a_0$ , such that galaxies dipping below equation (1) should have *larger*  $|\mathbf{a}_{\text{ext}}|$ . We investigate this issue in the next section.

For completeness, Fig. 5 shows the dependence of the distribution of  $|\mathbf{a}_{\text{ext}}|$  on the scale  $r_{\text{max}}$ , for the same mock galaxies used in Fig. 3. We see a slow rise that extends beyond  $r_{\text{max}} \gtrsim 90$  Mpc. We have also found that the correlation between  $\varepsilon$  and  $|\mathbf{a}_{\text{ext}}|$ , as measured by the Spearman coefficient, remains approximately constant with  $r_{\text{max}}$ .

## 4 COMPARISON WITH PREVIOUS RESULTS

In this section, we revisit the results of C20 who parametrised the departure of SPARC galaxy RARs from equation (1) by a dimensionless variable  $e$ , with positive values indicating downward deviations. We first recalculate the median  $e$  value reported by C20. We then ask whether the individual  $e$  values correlate with the external environment or with host halo masses.

We obtained  $e$  and  $e_{\text{env}} \equiv |\mathbf{a}_{\text{ext}}|/a_0$ , with  $a_0 = 1.2 \times 10^{-10} \text{ m s}^{-2}$  from the (corrected) Table 2 of Chae et al. (2021a). In what follows, we restrict attention to the 148 SPARC galaxies (of a total of 175) used by C20. In their final analysis, C20 selected a further subset of 113 galaxies by demanding that their baryonic accelerations  $x_0 \sim \log[a_{\text{bary}} (\text{m s}^{-2})]$  occupy the low acceleration regime, with each galaxy’s median  $x_0$  required to satisfy  $\langle x_0 \rangle \leq -10.3$ . This was motivated by the MOND expectation that departures of the RAR from equation (1) should occur only at low accelerations. From the CDM viewpoint, however, there is no reason to exclude data in this manner, so we will show results for the full sample as well as the low-acceleration subset.

### 4.1 Median value of $e$

The simple unweighted median of  $e$  values for the 113 low-acceleration galaxies is  $0.052 \pm 0.017$  (with the error estimated from 100 bootstrap samples). This agrees with the value and bootstrap error reported by C20. Similarly, the unweighted median of their corrected  $e_{\text{env}}$  values is  $0.033 \pm 0.001$ , in agreement with their reported median and error. However, these estimates do not account for measurement errors. Using inverse-variance weighting<sup>6</sup> to do so gives weighted medians

$$e = 0.008 \pm 0.017 \quad \text{and} \quad e_{\text{env}} = 0.026 \pm 0.002$$

for the *same* objects. These are important changes, since C20 used their significantly non-zero value of the median  $e$  and its statistical consistency with the median  $e_{\text{env}}$  to claim a statistical detection of the EFE for the low-acceleration sample. Our weighted median calculations, on the other hand, suggest that  $e$  is actually consistent with zero while  $e_{\text{env}}$  is not (although the large error on  $e$  means that it is still fully consistent with  $e_{\text{env}}$ ).

A similar analysis of the full set of 148 galaxies yields weighted (unweighted) median  $e = 0.008 \pm 0.013$  ( $0.039 \pm 0.014$ ), and  $e_{\text{env}} = 0.026 \pm 0.001$  ( $0.033 \pm 0.001$ ). I.e., as for the low-acceleration subset, the median  $e$  is consistent with zero. The heterogeneity of the SPARC sample, however, means that the errors quoted on individual  $e$  values can be substantially over- or under-estimated, making it essential to explore multiple avenues of statistical analysis (K.-H. Chae, private communication). While the downturn of the average RAR is visually apparent in fig. 3 of C20, and so the average  $e$  is likely to be non-zero, because the individual values of  $e$  are highly uncertain, quantifying it robustly is complicated.

### 4.2 Strength of and correlations with $\mathbf{a}_{\text{ext}}$

In addition to the uncertainty on the inferred average value of  $e$ , an important difference between our results and those of C20 is that their values of  $e_{\text{env}}$  are a factor  $\sim 4$  larger than those predicted by our  $\Lambda$ CDM mock (Fig. 3). Their  $\mathbf{a}_{\text{ext}}$  estimates were derived from a  $\Lambda$ CDM-based density reconstruction in the observed volume around the SPARC sample following

<sup>6</sup> We symmetrised the errors in  $e$  by defining  $\sigma_e = 0.5 \times (\sigma_+ + \sigma_-)$ , where  $\sigma_{\pm}$  are the upper and lower errors reported in the third column of Table 2 of Chae et al. (2021a). We similarly symmetrised errors in  $e_{\text{env}}$ . The errors in  $\log[m_{\text{vir}}]$  reported by Li et al. (2020) are already symmetric.

**D18.** Although not mentioned by C20, they used  $r_{\max} = 50$  Mpc rather than 10 Mpc for this analysis (H. Desmond, private communication). Since both our estimate and theirs are based on  $\Lambda$ CDM simulations, this discrepancy is *not* an issue of  $\Lambda$ CDM versus modified gravity. Fig. 5 shows that this also cannot be explained by the difference in  $r_{\max}$ ; we see that the median  $|\mathbf{a}_{\text{ext}}|$  increases by only a factor  $\sim 1.4$  from  $r_{\max} = 10$  Mpc to 50 Mpc. Rather, it can be traced back to the combination of two effects: (i) the use of untruncated NFW (henceforth, uNFW) profiles by D18 in their estimate of  $\mathbf{a}_{\text{ext}}$  and (ii) the selection of the SPARC sample.

To understand the effect of not truncating, it is useful to pretend that all the mass of a halo is concentrated into a point at its center. Then  $\mathbf{a}_{\text{ext}}$  is given by the first of the equalities in equation (9), except that the sum is now over halos, so  $m_{\text{part}}$  is replaced by  $m_h$  (different for each halo). The question is what to use for  $m_h$ . The mass within radius  $r$  around an uNFW profile diverges logarithmically as  $r \rightarrow \infty$ . So, for the  $i^{\text{th}}$  neighbour with radius  $R_i$  and concentration  $c_i$  at separation  $r_i$  from the galaxy in question, the assumption of an uNFW profile leads to a logarithmic enhancement of  $\sim \ln(c_i r_i / R_i) / \ln(c_i)$  to the mass, and hence to the contribution of this neighbour to  $\mathbf{a}_{\text{ext}}$ . For neighbours inside 10 Mpc with masses  $\gtrsim 10^{11} h^{-1} M_{\odot}$  as used by D18,  $\ln(c_i r_i / R_i) / \ln(c_i)$  is typically a factor of  $\sim 4$ , (and is about  $\sim 5$  when using  $r_{\max} = 50$  Mpc as in C20).

Of course, because halos below some threshold will not be observed, truncating the profiles of the objects which are observed, at say their virial radius is guaranteed to *underestimate* the actual mass distribution around the galaxy, since it neglects the mass in the environment between these neighbours. Thus, the uNFW assumption might coincidentally account for all mass reasonably well. To check, we repeated our analysis by replacing the sum over particles in equation (9) with a mass-weighted sum over haloes having  $m_{\text{vir}} \geq 7.7 \times 10^{10} h^{-1} M_{\odot}$  (close to the threshold used by D18), which gives us a point mass neighbour estimate for  $\mathbf{a}_{\text{ext}}$ . Multiplying this by a factor 4 gives an accurate approximation to the uNFW neighbour estimate used by D18. We find that the median  $|\mathbf{a}_{\text{ext}}|/a_0$  of this uNFW estimate is  $\sim 9.0 \times 10^{-3}$ , a factor  $\sim 1.5$  larger than our estimate using all the mass *for the same mock galaxies*: The uNFW assumption does overestimate  $|\mathbf{a}_{\text{ext}}|$ . This overestimate is further modified in the D18 method because they add to the halo-based mass distribution the contribution of a smoothed reconstruction based on Lagrangian perturbation theory (see their section 2.3).

Regarding sample selection, we note that the typical value of  $|\mathbf{a}_{\text{ext}}|/a_0$  inferred by D18 using the 2M++ sample (Lavaux & Hudson 2011) is  $\sim 0.013$  (see fig. 3b of D18), at least a factor 2 smaller than that inferred from the SPARC sample and a factor  $\sim 1.4$  larger than the ‘uNFW neighbour’ estimate using our mock catalog above. Since the SPARC and 2M++ analyses used essentially the same estimates of  $\mathbf{a}_{\text{ext}}$  from D18, their difference in typical  $|\mathbf{a}_{\text{ext}}|/a_0$  (apart from a factor  $\sim 1.4$  due to the different  $r_{\max}$  values, see above) must arise from differences in the underlying sample definitions (with SPARC being a biased subset of 2M++). Extending this reasoning to our mock catalog, we conclude that sample selection strategies make it difficult to compare our results for  $|\mathbf{a}_{\text{ext}}|/a_0$  with the existing literature to within a factor of 2.

A final interesting effect is that using the uNFW neighbour estimate as described above for our mock galaxies leads to a

Spearman correlation coefficient between  $\varepsilon \leftrightarrow |\mathbf{a}_{\text{ext}}|$  of  $\sim +0.18$  with negligible  $p$ -value, which is twice as strong as the one inferred using the particle-based estimate of  $\mathbf{a}_{\text{ext}}$ . This can be traced back to the fact that the neighbour-based  $|\mathbf{a}_{\text{ext}}|$  estimate correlates much more strongly with host mass  $m_{\text{vir}}$  than does the particle-based one (as Paranjape et al. 2018 note, there is substantial scatter between  $b_1$  and  $m_{\text{vir}}$ ). Thus, not only does the uNFW neighbour assumption overestimate the value of  $|\mathbf{a}_{\text{ext}}|$ , it also substantially overestimates the strength of the correlation between  $|\mathbf{a}_{\text{ext}}|$  and  $\varepsilon$ .

We conclude for now that we have a fair understanding of the difference between our calculation of  $|\mathbf{a}_{\text{ext}}|/a_0$  and the value inferred from the SPARC galaxies using the technique of D18. As mentioned previously, as far as estimation techniques are concerned, our particle counting technique is the more reliable, since it correctly accounts for all the mass surrounding the galaxy in question.

### 4.3 Correlation with $m_{\text{vir}}$

The results above indicate that the comparison between  $e$  and  $e_{\text{env}}$  in C20 is not robust. Therefore, we now focus on the  $e \leftrightarrow m_{\text{vir}}$  correlation, which is present in our  $\Lambda$ CDM mocks (c.f. Fig. 4, keeping in mind that our  $\varepsilon$  behaves qualitatively like  $-e$ ), and should not be affected by explicit environmental systematics. For this, we need  $m_{\text{vir}}$  estimates for the SPARC sample. We use the values from Li et al. (2020) which were obtained by fitting a cored NFW profile with  $\Lambda$ CDM priors on baryon-dark matter scaling relations to SPARC rotation curves. One caveat to be noted is that, for half of the sample of 148 objects,  $\chi^2/\text{dof} > 2$ , indicating a bad fit. (Some objects have an indeterminate  $\chi^2/\text{dof}$ .) Fitting with an Einasto profile gave only slightly better results (see their Fig. 1). The corresponding error estimates on the  $m_{\text{vir}}$  values, on the other hand, are typically small ( $\lesssim 0.1$  dex) for most objects. This feature of the Li et al. (2020) mass-modelling, namely, bad fits with small parameter errors, may indicate that the  $m_{\text{vir}}$  estimates are not reliable. The formalism and results presented in PCS21 and PS21 suggest that a self-consistent CDM analysis of rotation curves, especially for RAR studies, *must* include the effect of quasi-adiabatic relaxation, for example by allowing  $q_{\text{rdm}}$  (see section 3.1) to be a free parameter for each galaxy, in addition to halo mass, concentration and baryonic parameters. We will take up the required Monte Carlo fitting exercise in the near future. For now, we proceed using  $e$  estimates from C20 and  $m_{\text{vir}}$  estimates from Li et al. (2020), along with their respective errors, without modification.

Fig. 6 shows a scatter plot of  $e$  against  $\log[m_{\text{vir}}(M_{\odot})]$  for this sample, with the points used (excluded) by C20 shown in blue (red). We perform three statistical analyses to test for a correlation between these variables in the full sample as well as the low-acceleration subsample. The first is to ignore errors and calculate the Spearman rank correlation coefficient between  $e$  and  $m_{\text{vir}}$ . The values are reported in the labels in Fig. 6 and indicate no significant correlation. Next, we perform an orthogonal distance linear regression between  $e$  and  $\log[m_{\text{vir}}]$ , accounting for errors on both variables, using the `scipy.odr` numerical package. The results are shown as the red (blue) dashed line for all 148 (the 113 low-acceleration) galaxies, with a regression slope of  $0.022 \pm 0.008$  ( $0.05 \pm 0.01$ ) treating  $\log[m_{\text{vir}}]$  as the independent variable. Finally, we calculate the inverse variance-weighted median and central



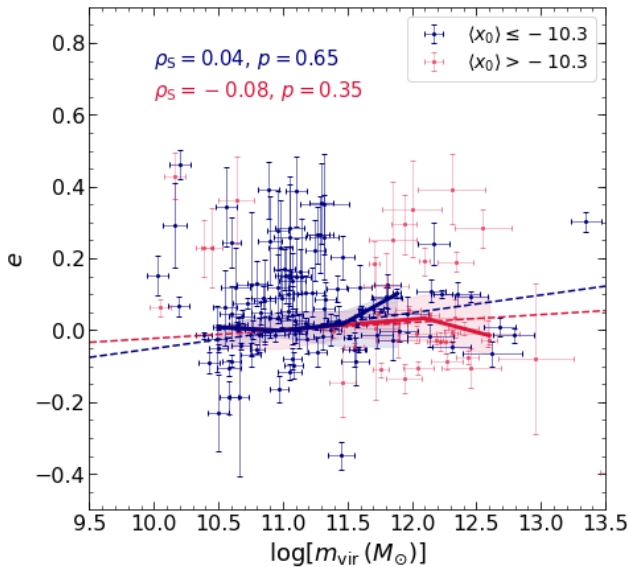


**Figure 6.** SPARC  $e$  against  $\log[m_{\text{vir}}]$ . Symbols show values and errors of  $\log[m_{\text{vir}}(M_{\odot})]$  reported by Li et al. (2020) and  $e$  reported by Chae et al. (2020), restricted to the 148 galaxies used by Chae et al. (2020). Blue points show the 113 objects having  $\langle x_0 \rangle < -10.3$  which were used for the EFE analysis by Chae et al. (2020, see their fig. 5), while red points show the remaining objects. Blue (red) label at the top shows the Spearman rank correlation coefficient  $\rho_S$  and associated  $p$ -value when using the blue symbols (all measurements) and ignoring errors. Dashed blue (red) line shows the result of orthogonal distance regression accounting for errors in both  $e$  and  $\log[m_{\text{vir}}]$  for the blue symbols (all measurements). Thick solid blue (red) line and associated band shows the weighted median along with weighted central 68% region of  $e$  in bins of  $\log[m_{\text{vir}}]$  for the blue symbols (all measurements). The weights were taken to be proportional to the inverse variance of each measurement, and the location of the points on the horizontal axis was chosen to be the weighted median of  $\log[m_{\text{vir}}]$  in each bin.

68% region of  $e$  in bins of  $\log[m_{\text{vir}}]$ , shown as a function of the weighted median  $\log[m_{\text{vir}}]$  in each bin by the solid curves with error bands using the same colour coding; these agree quite well with the linear regression.

Overall, we conclude that, when accounting for errors in both variables, there is a weak but significant positive trend detected between  $e$  and  $m_{\text{vir}}$  for the 113 low-acceleration galaxies, which substantially weakens for the full sample. A positive correlation is the opposite of what is predicted by the CDM framework, as we discussed in section 3.2 (there, *lower* mass implies a downward deviation, or positive  $e$ ). However, the fact that the trend in the full sample is weaker than in the low-acceleration subsample, along with the caveat regarding the reliability of the  $m_{\text{vir}}$  estimates and the uncertainties on the errors of the  $e$  values in the first place, suggests that this trend must be treated with caution. For now, we simply conclude that our results motivate a more self-consistent CDM analysis of the EFE in observed samples.

## 5 CONCLUSIONS

We have presented a simple, exact analytical calculation showing that, in the general relativistic CDM framework, it is

natural to expect a statistical correlation between the shape and/or amplitude of a galaxy’s RAR and the strength of the external gravitational field  $\mathbf{a}_{\text{ext}}$ . This by no means implies a violation of the strong equivalence principle, but emerges instead from the clustered nature of the distribution of galaxies and their surrounding mass.

We explicitly demonstrated this ‘external field effect’ (EFE) in a  $\Lambda$ CDM-based mock catalog of rotation curves of massive spiral galaxies, showing that the amount by which a galaxy’s RAR departs from the sample median ( $\varepsilon$  of equation 8) has a weak but significant positive correlation with its large-scale linear bias  $b_1$  and the estimated  $|\mathbf{a}_{\text{ext}}|$ , simply because  $\varepsilon$ ,  $b_1$  and  $\mathbf{a}_{\text{ext}}$  all correlate with the mass and concentration of the galaxy’s host halo. Thus, simply detecting a statistical EFE-like effect is *not* a conclusive test of GR. On the other hand, the *sign* of the EFE-like correlation in our mocks may provide a useful test. E.g., while MOND predicts that the  $\varepsilon \leftrightarrow |\mathbf{a}_{\text{ext}}|$  correlation is negative, in  $\Lambda$ CDM the sign of this correlation depends on  $m_{\text{vir}}$ : for stellar mass-selected samples, the sign is predicted to be positive. Moreover, in our mock catalog, the EFE-like  $\varepsilon \leftrightarrow b_1$  and  $\varepsilon \leftrightarrow |\mathbf{a}_{\text{ext}}|$  correlations vanish if measured at fixed mass and concentration. This vanishing may provide a better ‘null hypothesis’ in the search for unexpected ‘EFE’ effects. Of course, in the  $\Lambda$ CDM context, the tightness of the RAR means that unexpected EFE-like effects may provide an efficient way to search for ‘assembly bias’.

Finally, we argued that recent claims (C20) of a statistical EFE detection in the SPARC sample should be treated with caution. This is partly due to the large uncertainties associated with extracting the EFE signal from fits to the RAR of individual galaxies. We have also found that the values of  $|\mathbf{a}_{\text{ext}}|$  used by C20, which are determined following a  $\Lambda$ CDM-based Local Volume reconstruction from D18, are likely overestimated by at least a factor of  $\sim 1.5$ . More importantly, approximations made in numerically estimating  $\mathbf{a}_{\text{ext}}$  (such as the use of untruncated NFW profiles by D18) can spuriously enhance the correlation between  $|\mathbf{a}_{\text{ext}}|$  and EFE residuals extracted from the RAR. This must be accounted for in future studies of the EFE.

Our results not only motivate a more self-consistent treatment of mass-modelling of rotation curves within the CDM framework, properly accounting for the quasi-adiabatic relaxation of the dark matter in the presence of the baryons in a galaxy’s host halo, but also call for more robust estimates of the external gravitational field at the locations of Local Volume galaxies. This will require techniques that can access small-scale spatial information, e.g., those based on Voronoi tessellations of the galaxy distribution (Paranjape & Alam 2020); we will explore these in future work.

## ACKNOWLEDGMENTS

We thank K.-H. Chae for motivating us to study the external field effect in the CDM context, both he and H. Desmond for useful correspondence and comments on an earlier draft, and R. Srianand for useful discussions. The research of AP is supported by the Associateship Scheme of ICTP, Trieste and the Ramanujan Fellowship awarded by the Department of Science and Technology, Government of India. This work made extensive use of the open source computing packages

NumPy (Van Der Walt et al. 2011),<sup>7</sup> SciPy (Virtanen et al. 2020),<sup>8</sup> Matplotlib (Hunter 2007)<sup>9</sup> and Jupyter Notebook.<sup>10</sup>

## DATA AVAILABILITY

The mock catalogs underlying this work will be made available upon reasonable request to the authors.

## REFERENCES

- Battaglia G., Fraternali F., Oosterloo T., Sancisi R., 2006, *A&A*, **447**, 49
- Begum A., Chengalur J. N., 2004, *A&A*, **424**, 509
- Bekenstein J., Milgrom M., 1984, *ApJ*, **286**, 7
- Binney J., Tremaine S., 1987, *Galactic dynamics*. Princeton University Press, Princeton, NJ
- Boomsma R., Oosterloo T. A., Fraternali F., van der Hulst J. M., Sancisi R., 2008, *A&A*, **490**, 555
- Chae K.-H., Bernardi M., Sheth R. K., Gong I.-T., 2019, *ApJ*, **877**, 18
- Chae K.-H., Lelli F., Desmond H., McGaugh S. S., Li P., Schombert J. M., 2020, *ApJ*, **904**, 51
- Chae K.-H., Lelli F., Desmond H., McGaugh S. S., Li P., Schombert J. M., 2021a, *ApJ*, **910**, 81
- Chae K.-H., Desmond H., Lelli F., McGaugh S. S., Schombert J. M., 2021b, *ApJ*, **921**, 104
- Chemin L., Carignan C., Drouin N., Freeman K. C., 2006, *AJ*, **132**, 2527
- Desjacques V., Jeong D., Schmidt F., 2018, *Phys. Rep.*, **733**, 1
- Desmond H., Ferreira P. G., Lavaux G., Jasche J., 2018, *MNRAS*, **474**, 3152
- Faltenbacher A., White S. D. M., 2010, *ApJ*, **708**, 469
- Famaey B., McGaugh S. S., 2012, *Living Reviews in Relativity*, **15**, 10
- Giovanelli R., et al., 2005, *AJ*, **130**, 2598
- Guo H., Li C., Zheng Z., Mo H. J., Jing Y. P., Zu Y., Lim S. H., Xu H., 2017, *ApJ*, **846**, 61
- Haghi H., Bazkiaei A. E., Zonoozi A. H., Kroupa P., 2016, *MNRAS*, **458**, 4172
- Haghi H., et al., 2019, *MNRAS*, **487**, 2441
- Hu W., Kravtsov A. V., 2003, *ApJ*, **584**, 702
- Hunter J. D., 2007, *Computing In Science & Engineering*, **9**, 90
- Janz J., Cappellari M., Romanowsky A. J., Ciotti L., Alabi A., Forbes D. A., 2016, *MNRAS*, **461**, 2367
- Komatsu E., et al., 2011, *ApJS*, **192**, 18
- Lavaux G., Hudson M. J., 2011, *MNRAS*, **416**, 2840
- Lelli F., et al., 2015, *A&A*, **584**, A113
- Lelli F., McGaugh S. S., Schombert J. M., 2016, *AJ*, **152**, 157
- Lelli F., McGaugh S. S., Schombert J. M., Pawlowski M. S., 2017, *ApJ*, **836**, 152
- Li P., Lelli F., McGaugh S., Schombert J., 2020, *ApJS*, **247**, 31
- McGaugh S. S., Lelli F., Schombert J. M., 2016, *Phys. Rev. Lett.*, **117**, 201101
- Milgrom M., 1983, *ApJ*, **270**, 365
- Milgrom M., 1986, *ApJ*, **302**, 617
- Navarro J. F., Frenk C. S., White S. D. M., 1996, *ApJ*, **462**, 563
- Paranjape A., Alam S., 2020, *MNRAS*, **495**, 3233
- Paranjape A., Sheth R. K., 2021, *MNRAS*, **507**, 632
- Paranjape A., Hahn O., Sheth R. K., 2018, *MNRAS*, **476**, 3631
- Paranjape A., Choudhury T. R., Sheth R. K., 2021, *MNRAS*, **503**, 4147
- Paul N., Choudhury T. R., Paranjape A., 2018, *MNRAS*, **479**, 1627
- Paul N., Pahwa I., Paranjape A., 2019, *MNRAS*, **488**, 1220
- Ramakrishnan S., Paranjape A., Hahn O., Sheth R. K., 2019, *MNRAS*, **489**, 2977
- Ramakrishnan S., Paranjape A., Sheth R. K., 2021, *MNRAS*, **503**, 2053
- Schneider A., Teyssier R., 2015, *J. Cosmology Astropart. Phys.*, **2015**, 049
- Teyssier R., Moore B., Martizzi D., Dubois Y., Mayer L., 2011, *MNRAS*, **414**, 195
- Tian Y., Umetsu K., Ko C.-M., Donahue M., Chiu I. N., 2020, *ApJ*, **896**, 70
- Van Der Walt S., Colbert S. C., Varoquaux G., 2011, preprint, ([arXiv:1102.1523](https://arxiv.org/abs/1102.1523))
- Virtanen P., et al., 2020, *Nature Methods*, **17**, 261
- Wechsler R. H., Zentner A. R., Bullock J. S., Kravtsov A. V., Allgood B., 2006, *ApJ*, **652**, 71
- York D. G., et al., 2000, *AJ*, **120**, 1579
- Zehavi I., et al., 2011, *ApJ*, **736**, 59

<sup>7</sup> <http://www.numpy.org>

<sup>8</sup> <http://www.scipy.org>

<sup>9</sup> <https://matplotlib.org/>

<sup>10</sup> <https://jupyter.org>